ENHANCED MODEL OF GEAR TRANSMISSION DYNAMICS FOR CONDITION MONITORING APPLICATIONS: EFFECTS OF TORQUE, FRICTION AND BEARING CLEARANCE

A. Fernandez-del-Rincon, P. Garcia, A. Diez-Ibarbia,
A. de-Juan, M. Iglesias, F. Viadero

Department of Structural and Mechanical Engineering, University of Cantabria. Avda. de los Castros s/n 39005 Santander, Spain.

Abstract

Gear transmissions remain as one of the most complex mechanical systems from the point of view of noise and vibration behavior. Research on gear modeling leading to the obtaining of models capable of accurately reproduce the dynamic behavior of real gear transmissions has spread out the last decades. Most of these models, although useful for design stages, often include simplifications that impede their application for condition monitoring purposes. Trying to filling this gap, the model presented in this paper allows to simulate gear transmission dynamics including most of these features usually neglected by the state of the art models.

This work presents a model capable of considering simultaneously the internal excitations due to the variable meshing stiffness (including the coupling among successive tooth pairs in contact, the non-linearity linked with the contacts between surfaces and the dissipative effects), and those excitations consequence of the bearing variable compliance (including clearances or pre-loads). The model can also simulate gear dynamics in a realistic torque dependent scenario.

The proposed model combines a hybrid formulation for calculation of meshing forces with a non-linear variable compliance approach for bearings. Meshing forces are obtained by means of a double approach which combines numerical and analytical aspects. The methodology used provides a detailed description of the meshing forces, allowing their calculation even when gear center distance is modified due to shaft and bearing flexibilities, which are

unavoidable in real transmissions. On the other hand, forces at bearing level were obtained considering a variable number of supporting rolling elements, depending on the applied load and clearances. Both formulations have been developed and applied to the simulation of the vibration of a sample transmission, focusing the attention on the transmitted load, friction meshing forces and bearing preloads.

Keywords: Gear, Model, Transmission Error, Load Ratio, Meshing Stiffness, Finite Element, Bearings, Condition Monitoring

---

Nomenclature

F_i Force acting on contact point i

K_m Meshing stiffness

Z_i Teeth number of wheel i

χ_i curvature radius of the contacting surface

δ Geometric overlap

η Dynamic Viscosity

$\lambda_{i,k}$ Deformation of the contact point i when a unitary force is applied at the contact point k

ad Addendum

f Friction coefficient

h Frontier depth for the superposition of problems

m Module

n Number of actual contact points

BPF Ball Pass Frequency

DOF Degrees of Freedom

DTE Dynamic Transmission error

FE Finite Element

GMF Gear Mesh Frequency

LOA Line Of Action

OLOA Out of the Line Of Action

c Bearing Clearance

1. Introduction

Gear transmissions remain as one of the most complex mechanical systems from the point of view of noise and vibration behavior. They are applied in several ways i.e. for speed changes, for torque gain, torque reduction or power split among others. The future foresees higher torque levels with a global increment in the power density, a reduction in energy consumption, better endurance and lower noise and vibration levels [1]. To cover these demands the industry should carry out a great effort on understanding the dynamics of these kinds of systems. In order to achieve this task, better theoretical models should be developed, which might be able to accurately reproduce the dynamic behavior of real gear transmissions.

Moreover, gear transmissions are critical components on a wide range of machinery i.e. helicopter transmissions, wind turbines and aerospace applications having a great impact on the final success of the whole system. As an example, in the case of wind turbines, gearboxes represent an important percentage of the final cost of the machinery but they are also a component especially susceptible to develop expensive failures, which have a great impact on the final profit in operation [2].

Therefore, besides its utility on the improvement of the gear transmissions design stage, the development of specific models capable to reproduce the dynamic behavior in operation, arise as a very interesting goal to their application in condition monitoring applications. This possibility has been suggested by some researchers such as Bartelmus [3], who proposed the use of a model of gear transmissions as an aid for diagnostics or Ho and Randall [4] who applied these kinds of tools for the case of bearings. Following this approach, during last years several authors have addressed the simulation of different kinds of faults in gear transmissions, such as gear cracks [5],[6],[7], tooth breakage [8], surface pitting and/or spalling [9], [10], among others.

However, most of these models tend to present a lot of simplifications, without a detailed description of the most critical aspect involved in gear dynamics, which is the role played by the parametric excitation due to the variable number of meshing tooth pairs [11], as well as its inherent non-linearity.

On top of the variable meshing stiffness, gear transmissions are usually supported by rolling bearings, which undergo the same kinds of dynamic phenomena described for gears: a parametric excitation due to the variable number of rolling elements transmitting the load to the support. This variation in the number of rolling elements effectively supporting the load causes a variable stiffness in the bearings, and will result in the appearance of vibrations. These vibrations are characterized by multiples of the so-called Ball Pass Frequency (BPF) which is obtained as the product of the number of rolling elements by the cage rotation frequency. The consideration of the variable stiffness due to the angular position of the cage, and therefore of different number of contacting elements, was proposed by Gupta [12]. Later, Fukata *et al.* [13] developed a two-dimensional model including the effects of clearances, contact stiffness and parametric excitation. Nevertheless, the inclusion of bearing flexibility in gear dynamic models has been simply approached by considering bearings as time invariant flexible supports [14].

On the other hand, a reduced number of researchers have proposed advanced models combining gear and roller bearing dynamics, including the parametric excitation due to both elements in order to analyze the interaction between these elements and its consequences on the dynamics and vibratory behavior. An interesting example is the model proposed by Lahmar and Velex [15], who combines the gear model developed in [16] with a non-linear formulation for ball and roller bearings including the variable compliance of these elements. This formulation was linearized carrying out static and dynamic analysis in order to compare the results obtained with the original non-linear approach. Moreover, Sawalhi and Randall [17] developed a model for spur gear transmissions, focusing their attention on the inclusion of ball bearings with several types of faults.

Nevertheless, real transmissions present some features usually neglected in the mentioned models, such as the coupling among successive tooth pairs in contact and the non-linearity linked with the contacts between surfaces. These phenomena have implications in the load sharing between teeth pairs, and as a consequence in the actual contact ratio, due to the fact that the deformation values will be greater than the estimated ones from purely kinematic approaches, as those applied in previous models. Furthermore, shafts and bearings interact with gears, increasing the complexity of transmission dynamics. Depending on the level of the transmitted torque, those elements suffer deflections and hence the gear center distance becomes greater. Thus, the tooth engagement process is modified and consequently the meshing stiffness provides a different dynamic response for different torque levels. As a consequence, transmissions working under different load conditions result in a problem for conventional condition monitoring applications, as the alarm levels and the system set up must consider several working conditions.

Aiming to cover this gap, the authors developed an advanced model, combining rolling bearings and gears, for quasi-static analysis [18] showing the consequences in gear centre orbits, transmission error and meshing stiffness when several levels of transmitted torques are applied. The computational features of the procedure for calculation of meshing forces based on a hybrid approach combining numerical and analytical tools, were presented in [19] and subsequently applied on the quasi-static simulation of tooth defects like pitting and tooth cracks [20]. Afterwards, in [21] the model was extended to dynamic analysis and applied to simulate the impact of profile deviations, while in [22] index and run out errors were considered. This paper describes the enhancement of the model towards on condition monitoring applications by showing the interaction between the non-linear behavior of bearing and gears, assessing the consequences of meshing friction, bearing clearances and the level of the applied torque.

2. Model Description and Dynamic Equations

Figure 1 illustrates a schema of the sample transmission used, consisting of a couple of spur gears mounted on elastic shafts, which are supported by two ball bearings each. Each wheel is modeled as a rigid disk with lumped inertia at the center, under the assumption of plane motion, considering two translational Degrees Of Freedom (DOF) and one rotational. Both gears are mounted on flexible shafts allowing in plane deflection and torsion. Furthermore, each shaft is supported by two bearings, whose inertia is also lumped at their center adding three more DOF for each one. The connection between components is done by a linear translational/rotational spring with a viscous damper or by a non-linear function (represented in Figure 1 by springs-dampers and double sense arrows respectively) related with the behavior of gears and bearings. Normal surface meshing contact forces are obtained by a hybrid approach, combining numerical and analytical methods. Moreover, dissipative phenomena, as friction and oil damping, are added to improve the capabilities of the model, as described in the next section.

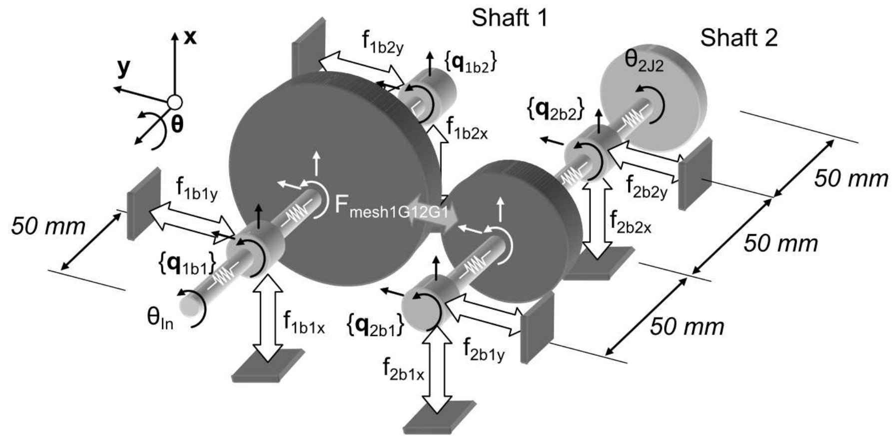

Figure 1: Schema of the gear transmission

Bearing forces are included by considering the angular variable compliance due to the change in the number of rolling elements supporting the load. Meanwhile, bearing damping is added as an equivalent translational viscous damping, which has the same value for any direction on the plane of movement (torsional damping is not considered). In order to define the transmitted torque by the system, the input rotational speed and the output torque must be defined. This agrees with the assumption of a constant load at the output and a speed controller on the drive at the input. To set up this approach, an additional rotational inertia is included at the output, where a torque is applied to load the transmission. Taking a reference frame, with the z-axis oriented along the shaft center line and the y-axis defined by the line between gear centers, x and y are the translational degrees of freedom along the x and y-axis while θ is the rotational degree of freedom around the z-axis. Each degree of freedom is identified with a subscript with the form iEj, where i denotes the shaft number of the element of interest, E is a subscript to distinguish between bearings (subscript b), gears (subscript G) and rotational inertia (subscript J), and j denotes the element number among those located in the same shaft. As an example, x_{ibj} means the displacement along the x-axis of bearing j belonging to shaft i. Moreover, the degrees of freedom associated with bearings and gears are grouped in vectors $\mathbf{q}_{ibj} = \{x_{ibj}, y_{ibj}, \theta_{ibj}\}^T$ and $\mathbf{q}_{iGj} = \{x_{iGj}, y_{iGj}, \theta_{iGj}\}^T$. Then, the mass, damping and stiffness matrices for the whole system (shafts, gears and bearings) are assembled into the dynamic matrix equation, arriving at a system with 19 DOF (the input rotation is known) which expressed in matrix form gives rise to the following expression:

$$\begin{aligned} &\mathbf{M}\ddot{\mathbf{q}} + \mathbf{C}\dot{\mathbf{q}} + \mathbf{K}\mathbf{q} + \mathbf{f}_b(\mathbf{q}) + \mathbf{f}_G(\mathbf{q}, \dot{\mathbf{q}}) = \mathbf{f}_{Ext}(t); \\ &\mathbf{q} = \{\mathbf{q}_{1b1}, \mathbf{q}_{1G1}, \mathbf{q}_{1b2}, \mathbf{q}_{2b1}, \mathbf{q}_{2G1}, \mathbf{q}_{2b2}, \theta_{Out}\}^T; \end{aligned} \tag{1}$$

Non-linear terms due to bearings and gears are included in vectors $\mathbf{f}_b$ and $\mathbf{f}_G$, while matrices $\mathbf{M}$, $\mathbf{C}$ and $\mathbf{K}$ are constant coefficient matrices. The detailed dynamic equations are presented in Annex A.

3. Meshing Forces

For this purpose, in this work a hybrid procedure has been applied by combining numerical and analytical formulations [23], [24] and [25]. This procedure divides the gear contact into two regions: the surroundings of the contact and the rest of the gear body. The deflection in the region close to the contact is defined by an analytical formulation, while the deflection away from the contact is obtained by a numerical FE model. The main advantage of this approach is that it is not necessary to develop a new FE model with refined mesh for each contact position. Furthermore, its use reduces the computational effort, as the FE model analysis becomes linear, whilst the non-linear problem related to the surface contact is simplified by the analytical formulation.

Following this approach, assuming F_n forces on n contacting points located at successive teeth couples, the total displacement of the $i-th$ contact point (u_{Ti}) is obtained by the addition of the non-linear terms due to the local deflection of each contacting surface (u_{Li}) and due to the global deflection, which is expressed as a linear combination of all the contact forces involved in the meshing position analyzed.

Thus, the meshing forces F_i are found solving the non-linear system shown in Eq.(2), attending to two conditions. The first is the condition of compatibility, which states that the sum of deflections of conjugated teeth (u_{Ti}) must be equal to the interference value due to rigid-body displacements of the wheels (δ_i). The second is the complementary condition, which assures that negative loads are not considered at the points where real contact does not take place.

$$\left\{\begin{array}{l}\delta_1(\mathbf{q}_p,\mathbf{q}_w)\\ \delta_2(\mathbf{q}_p,\mathbf{q}_w)\\ ...\\ \delta_n(\mathbf{q}_p,\mathbf{q}_w)\end{array}\right\} = \left\{\begin{array}{l}u^p_{L,1}\left(\mathbf{q}_p,\mathbf{q}_w,F_1\right)\\ u^p_{L,2}\left(\mathbf{q}_p,\mathbf{q}_w,F_2\right)\\ ...\\ u^p_{L,n}\left(\mathbf{q}_p,\mathbf{q}_w,F_n\right)\end{array}\right\} + \left\{\begin{array}{l}u^w_{L,1}\left(\mathbf{q}_p,\mathbf{q}_w,F_1\right)\\ u^w_{L,2}\left(\mathbf{q}_p,\mathbf{q}_w,F_2\right)\\ ...\\ u^w_{L,n}\left(\mathbf{q}_p,\mathbf{q}_w,F_n\right)\end{array}\right\} + \\ + \left(\left[\boldsymbol{\lambda}^w\left(\mathbf{q}_p,\mathbf{q}_w\right)\right] + \left[\boldsymbol{\lambda}^p\left(\mathbf{q}_p,\mathbf{q}_w\right)\right]\right)\left\{\begin{array}{c}F_1\\ F_2\\ ...\\ F_n\end{array}\right\} \\ F_i \geq 0; \qquad i=1,...,n \tag{2}$$

Where superscript w and p stands for wheel and pinion, and $\lambda_{i,k}$ represents the flexibility influence coefficients. Regarding local deformations, the displacement between a point on the surface of a solid and a point located at a depth h is obtained according to the expression derived by Weber-Banashek [25] for bi-dimensional plane strain problems. On the other hand, the flexibility influence coefficients ($\lambda_{i,k}$) represent the displacement of the contact point i when a unitary force is applied at point k and are obtained from a linear FE analysis.

Therefore, this method provides the meshing forces F_i for any particular position of the gears and torque load, considering translational motion due to flexibility of bearings and shafts and as a consequence changes in the center distance, pressure angle and contact ratio. The procedure summarized in this section is described in more detail in [19], where it is also presented the validation of the meshing stiffness values by means of comparison with the ISO norm. Also in [26] the model behavior is compared in terms of meshing stiffness with other published approaches obtaining good correspondence. From the experimental point of view, the presented model has also been put to test in [27], where the results are further confirmed.

4. Gear meshing dissipative effects

In order to enhance the original model increasing its features for accurate simulation of gear dynamics, meshing forces have been furthermore extended to include friction and damping effects. Regarding friction, He [28] concluded that different models with a variety of complexity levels provide very similar results about the predicted motions in the Line Of Action (LOA). Hence, in this work it has been assumed a Coulomb model with constant friction coefficient, using a smothering function to avoid numerical problems due to the discontinuity on the friction force when the contact arrives to the pitch point, according to the following expression:

$$\begin{aligned}(\mathbf{F}_f)_i^P &= -F_i f \tanh\left(\frac{\left|\mathbf{v}_{P_i(P/W)}\cdot\mathbf{t}_i\right|}{v_0}\right)\operatorname{sgn}(\mathbf{v}_{P_i(P/W)}\cdot\mathbf{t}_i)\cdot\mathbf{t}_i\\ (\mathbf{F}_f)_i^W &= -\left(\mathbf{F}_f\right)_i^P\end{aligned} \tag{3}$$

Where $(\mathbf{F}_f)_i^P$ and $(\mathbf{F}_f)_i^W$ are the friction force vectors at the i contact for pinion and wheel respectively, f is the friction coefficient, F_i is the contact force at the i contact, $\mathbf{v}_{P_i(P/W)}$ is the relative velocity between the contacting points on pinion and wheel tooth surface, $\mathbf{t}_i$ is a unitary vector which defines the common tangent to the contacting surfaces, and v_0 is a threshold level to smooth the transition when the relative velocity is null.

The inclusion of damping in gear dynamic models has not been addressed in a clear and homogeneous way through the literature, being difficult to find works that adequately explain this phenomenon which in fact involves several mechanisms. In the case of lumped models, most authors consider that the damping due to the gear meshing can be represented by a viscous model, defined by a equivalent damping coefficient C acting on the torsional degrees of freedom [29]. More recently, some authors have included in their models the effect of the lubricant surrounding the contacting surfaces [30]. Mucchi *et al.* [31] develop a more complex formulation, considering two damping sources at meshing contacts, one due to the hysteresis damping consequence of teeth flexion and Hertzian deflections and one other due to the oil squeeze effect.

In this work, both hysteretic and oil squeeze contribution are considered, neglecting other sources such as oil churning. Following this assumption, the damping force $\mathbf{F}_{Di}$ for the contact i was defined by the expression:

$$\begin{aligned}(\mathbf{F}_D)_i^P &= -C_{D_i}\left(\mathbf{v}_{P_i(P/W)}\cdot\mathbf{n}_i\right)\mathbf{n}_i\\ (\mathbf{F}_D)_i^W &= -\left(\mathbf{F}_D\right)_i^P\end{aligned} \tag{4}$$

Where $\mathbf{n}_i$ is the common normal to the pinion and wheel surfaces corresponding to the contact i, while the damping coefficient C_D is derived from:

$$C_D = \begin{cases} 2\xi\sqrt{\bar{K}_{Mesh}M_{Eq}} & F_i > 0 \\ 12\pi\eta b\left(\frac{1}{2\max(\delta_{Threshold},\delta_i)}\frac{\chi_P\chi_W}{\chi_P+\chi_W}\right)^{3/2} & F_i = 0 \end{cases} \tag{5}$$

Thus, when the contact is active, the corresponding force F_i is not null and the hysteretic damping model defined by Eq.(3) is switched on. Otherwise, the profiles are not in contact and the formulation proposed by Koster [32] is applied. There, η is the dynamic viscosity, b is the gear width, δ_i is the gap between tooth profiles and χ_i $(i = P, W)$ is the curvature radius of the contacting surface i.

5. Ball Bearing Contact Forces

Bearings forces have been obtained by means of the approach proposed by Fukata *et al.* [13], based on the following assumptions:

- Both inner and outer races are considered rigidly attached to the shaft and the frame respectively.
- All elements of the bearing are rigid, so that the only possible deformation is related to contacts between rolling elements and inner and outer races.
- These contacts allow the application of the Hertzian theory.
- The average angular position of the rolling element is defined by the cage, whose angular location is obtained by considering pure rolling without slipping at the contacts with inner and outer races. Nevertheless a random variation on the angular location of each rolling element can be considered.

According to the last assumption, the cage angular position (θ_{Cage}) can be obtained from the angular position of inner (θ_{In}) and outer (θ_{Out}) races by:

$$\theta_{Cage} = \frac{\theta_{In}}{2}\left(1 - \frac{d}{D}\cos(\alpha)\right) + \frac{\theta_{Out}}{2}\left(1 + \frac{d}{D}\cos(\alpha)\right) \tag{6}$$

Where D is the average value of the projected inner and outer diameters in the bearing transverse plane, d is the diameter of rolling element and α is the contact angle.

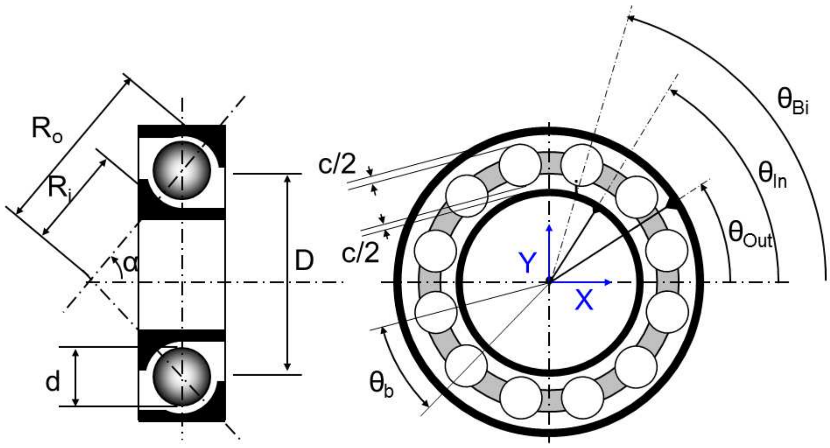

Figure 2: Rolling bearing parameters scheme

Usually, the outer race is stationary and Eq.(6) can be particularized assuming a null value for θ_{Out}. Under this assumption, the angular position of the rolling element i (θ_{REi}) is determined from:

$$\theta_{REi} = \frac{2\pi}{N_b}(i-1) + \frac{\theta_{In}}{2}\left(1 - \frac{d}{D}\cos(\alpha)\right) + \theta_0 \tag{7}$$

Here, N_b is the number of rolling elements and θ_0 is the cage angular offset with respect to the reference position, which corresponds with a rolling element located on the positive horizontal axis (X) defined in Figure 2. Then, considering the cartesian reference system defined in Figure 2 and assuming that the outer race is fixed, the total radial overlap (δ_{REi}) between the i^{th} rolling element, defined by its angular position (θ_{REi}), and the inner and outer tracks are a function of the coordinates (x, y), which defines the location of the inner race center and the bearing radial clearance c, according to the expression:

$$\delta_{\theta_{REi}} = x\cos(\theta_{REi}) + y\sin(\theta_{REi}) - c; \qquad i = 1, 2, ...N_b \tag{8}$$

Then, contact forces are obtained from the hypothesis of Hertzian contact, leading to a non-linear relationship between the resultant force on the rolling element i and the total radial overlap ($\delta_{\theta_{REi}}$). Imposing the condition of complementarity, by means of the Heaviside function $H()$, so that there is only contact in those cases in which the radial deformation is positive, the resultant force, projected in the horizontal (x) and vertical (y) direction, is obtained by:

$$
\begin{aligned}
F_x &= k_{RE}\sum_{i=1}^{N_B} H(\delta_{\theta_{REi}})\delta_{\theta_{REi}}^{p}\cos(\theta_{REi}) \\
F_y &= k_{RE}\sum_{i=1}^{N_B} H(\delta_{\theta_{REi}})\delta_{\theta_{REi}}^{p}\sin(\theta_{REi})
\end{aligned}
\qquad
H(\delta_{\theta_{REi}})\begin{cases} 1 & \delta_{\theta_{REi}} \geq 0 \\ 0 & \delta_{\theta_{REi}} < 0 \end{cases}
\tag{9}
$$

Where k_{RE} is the stiffness obtained by serial composition of Hertzian stiffness due to contact with inner and outer races and p is the non-linear exponent, which is 1.5 for balls and 1.1 for rollers. Details regarding the procedure for calculation of k_{RE} can be found in Annex B.

6. Numerical Simulations

In the following, the model described in the previous sections has been applied to simulate the dynamic behaviour of a sample gear transmission defined by the parameters shown in Tables 1 to 3 . Table 1 lists the values corresponding to the gear parameters of the mathematical model described in the previous sections. Each gear is mounted in a shaft supported by a pair of 209 single-row radial deep-groove ball bearings with the geometrical dimensions presented in Table 2. Table 3 contains the information related to the shaft stiffness and damping.

Table 1: Gear data

Parameter	Value	Parameter	Value
Number of teeth	28	Rack tip rounding	0.25 m
Module (m)	3.175 [mm]	Gear tip rounding	0.05 m
Elasticity Modulus	210 [GPa]	Rack dedendum	1 m
Poisson's ratio	0.3	Rack ad	1.25 m
Pressure angle	20 [degree]	Oil dyn. viscos.	0.004[Pa s]
Gear face width	6.35 [mm]	$m_{1G1} = m_{2G1}$	0.79999 [kg]
Gear shaft radius	20 [mm]	$J_{1G1} = J_{2G1}$	4.0408 10^{-4} [Kg m^2]

Although the proposed model allows for the simulation of transient conditions, in the examples presented in this paper only stationary conditions were considered, with the aim of isolate and better demonstrate the model capabilities. Particularly, all simulations have been done using a constant rotational speed of 1000 rpm at the input shaft, loaded with several stationary torques ranging from 10 to 100 Nm. Numerical integration of dynamic equations was approached using a SIMULINK® fixed step solver (*ode3 Bogacki-Shampine*)

Table 2: Bearing paramenters (209 single-row radial deep-groove ball bearing [33])

Parameter	Value
Outer race diameter (Ro)	77.706 [mm]
Groove radius of outer-ring (ro)	6.6 [mm]
Rolling element diameter (d)	12.7 [mm]
Inner race diameter (Ri)	52.291 [mm]
Groove radius inner-ring (ri)	6.6 [mm]
Radial clearance (c)	0.015 [mm]
Bearing Mass; $m_{1b1} = m_{2b2}; (m_{1b2} = m_{2b1})$	0.4901 (0.245) [kg]
Bearing Inertia; $J_{1b1} = J_{2b2}; (J_{1b2} = J_{2b1})$	9.9 10^{-5} (4.9 10^{-5}) [Kg m^2]
Number of Rolling Elements (Nb)	9

Table 3: Dynamic properties of connecting shafts

Parameter	Value
Output Inertia; J_{2J2}	3.56 10^{-4} [Kg m^2]
Coupling Stiff.; $K_{T1J1b1} = K_{T2b2J2}$	4.0 10^5 [Nm/rad]
Coupling Damp.; $C_{T1J1b1} = C_{T2b2J2}$	3.5761 [Nms/rad]
Bearing Damping; $C_{1b1} = C_{1b2} = C_{2b1} = C_{2b2}$	334.27 [Ns/m]
Shaft flex. Stiff.; $K_{1b1G1} = K_{1G1b2} = K_{2b1G1} = K_{2G1b2}$	6.24 10^8 [N/m]
Shaft Tor. Stiff.; $K_{T1b1G1} = K_{T1G1b2} = K_{T2b1G1} = K_{T2G1b2}$	4.0 10^5[Nm/rad]
Shaft Flex. Damp.; $C_{1b1G1} = C_{1G1b2} = C_{2b1G1} = C_{2G1b2}$	31.6 [Ns/m]
Shaft Tor. Damp.; $C_{T1b1G1} = C_{T1G1b2} = C_{T2b1G1} = C_{T2G1b2}$	0 [Nms/rad]

with a sampling frequency of 75 kHz. In order to reduce the transient period, simulations were launched taking as initial conditions the position of gears and bearings derived from a previous quasi-static equilibrium problem which was obtained by neglecting velocity and acceleration terms in Eq.(1).

The non-linear problem was solved numerically for a certain torque at the output and several angular positions for the driving gear up to complete the entire bearing cycle. The resulting orbits for bearings $1b1$ and $2b1$ centers corresponding to the example for output torques ranging from 10 to 100 Nm are presented in Figure 3, where the dashed line represents the corresponding value of the bearing clearance (c). In this figure it can be appreciated how the orbits are disposed along the LOA with a larger displacement Out of the Line Of Action (OLOA), even though friction was not considered in this analysis. This feature is due to the fact that bearing stiffness in the LOA is higher than the one in OLOA, as a consequence of the bearing clearance. Moreover, the amplitude of the displacement in OLOA is shorter for the extreme torque values, while intermediate torques (between 30 to 60 Nm) provide larger courses. This behavior is due to the non-linear nature of the bearing model, which provides a rising number of rolling elements supporting the load as the applied force is increased. Gear center orbits are similar to that shown for bearing $b11$, but shifted in the LOA due to the shaft deflection.

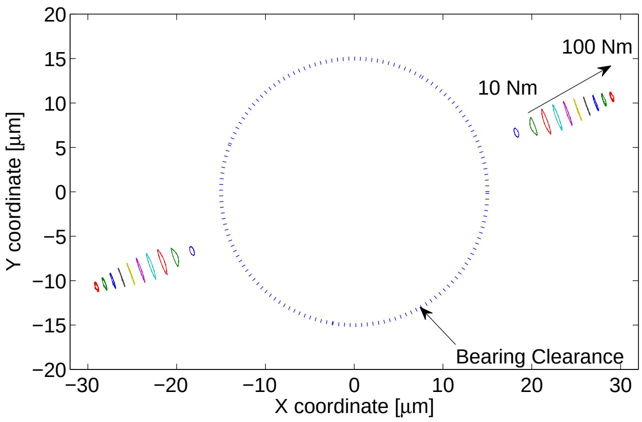

Figure 3: Bearings $1b1$ and $2b1$ center orbits for several torque values. Dashed line depicts bearing clearance

6.1. The effect of torque load

As it was described in the previous sections, a great number of the models for simulation of gear dynamics use a simple formulation for meshing forces commonly based on gear rigid body kinematics, neglecting the role of the transmitted torque in the analysis, with has important consequences on the transmission behavior. Although these approaches do not lead to very different dynamic behavior in the global sense (since the vibration *rms* level remains very similar), however the time record and therefore the corresponding frequency spectrum will be different, which has huge implications when on condition monitoring is the goal of the model. On the contrary, the procedure described in this paper avoids this drawback extending the model capabilities for multi-load simulations and providing more advanced capabilities (i.e. bearing variable compliance, friction, gear defects, lubricant damping, etc.) useful in the context of condition monitoring.

With the aim of comparing and assessing the advantages of the proposed approach over conventional models, the quasi-static analysis was furthermore extended in order to determine the meshing stiffness along a cycle. With this objective, it was decided to pre-calculate the stiffness values for each of the considered potential contacts, exploiting the advantages of the original procedure. Thus, once the orbits are known, their centroids (midpoint for the orbit described by each gear center was determined from the orbits in a bearing cycle) are calculated and a new quasi-static analysis is done, fixing the gear center position to said centroids. During this analysis, the contact forces and the profile geometrical interferences are obtained, defining the meshing stiffness for each potential contact along a meshing cycle as a function of the angular position of the driving gear. In this way, relevant information provided by the model was preserved while its overall structure remains unchanged.

The resulting meshing stiffness values under several torque loads can be then stored to be used subsequently in dynamic simulations. Figure 4 shows the results obtained for the example transmission when two different values of transmitted torque are considered (10 and 100 Nm). The increase in the transmitted torque leads to the extension of the meshing period with a couple of teeth pairs in contact.

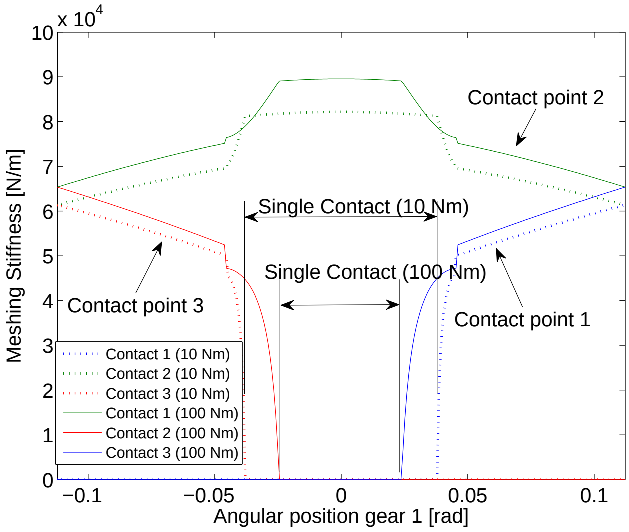

Figure 4: Meshing Stiffness for successive teeth contacts for two levels of transmitted torque (Dashed line 10 Nm; Solid line 100 Nm)

Once completed the calculation of individual meshing stiffness, the original model was applied to assess the consequences of a wrong formulation of meshing stiffness and to understand its influence on the simulated behaviour. In order to do that, three analysis were done for the example transmission considering a rotational speed of 1000 rpm and a torque of 100 Nm. The first one, hereinafter called A, was carried out using the original dynamic model. A second one, called B, was done under the same torque of 100 Nm but using pre-calculated stiffness corresponding to the same torque (100 Nm). Finally, the third one, designed as C, was done again with a torque of 100 Nm but this time using a pre-calculated stiffness obtained under a torque of 10 Nm. In this way, case C could be considered similar to the conventional torque-independent models. With the aim of comparison, the Dynamic Transmission Error (DTE) was obtained for each simulation according to the following expression:

$$DTE(t) = \theta_{1G1}(t) - \frac{Z_2}{Z_1}\theta_{2G1}(t); \tag{10}$$

Where, Z_i represents the number of teeth for each gear, which in the example analyzed are the same. Figure 5 shows the resulting DTE for each model corresponding to five meshing cycles. There, the differences between models become clear: while the model with pre-calculated stiffness based on a torque of 100 Nm gives a DTE with very small differences with respect to the model without pre-calculation, the model based on a pre-calculated meshing stiffness under a torque of 10 Nm provides a completely different response, tending to overestimate the resultant DTE amplitude.

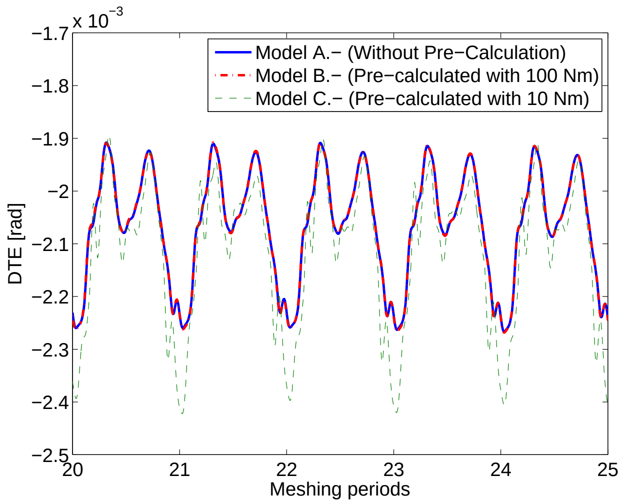

Figure 5: DTE obtained under different assumptions for Meshing Stiffness (K_m) Calculation

The differences are even more evident when the spectral decomposition of the resulting LOA force transmitted by the bearing (identified as 1b1 in Figure 6) is considered. Once again, the model with pre-calculated meshing stiffness using the appropriate torque of 100 Nm (Figure 6(b)) practically provides the same results as the model without pre-calculation shown in Figure 6(a), with negligible differences on the harmonics amplitude. On the other side, the model simulated using a wrong estimation of the meshing stiffness, based on the pre-calculated values obtained for a torque of 10 Nm, provides a spectrum (Figure 6(c)) completely different, particularly overestimating the 4^{th} and 5^{th} harmonic of the Gear Mesh Frequency (GMF).

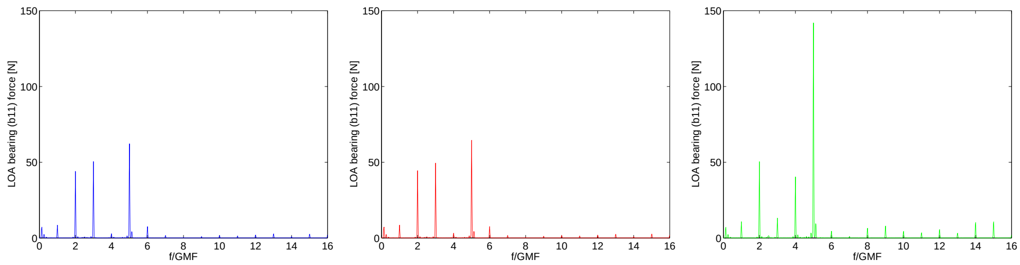

(a) Model A (without pre-calculation) (b) Model B (pre-calculated using 100 Nm) (c) Model C (pre-calculated using 10 Nm)

Figure 6: Spectrum of the LOA force in the support 1b1 (1000 rpm, 100 Nm)

Therefore, the use of simplified models with pre-calculated values for the contacting stiffness can be useful in dynamics simulations, providing the same results as those from more complex models with a shorter computation time. However, if what is required is an accurate estimate of the behavior under certain operating conditions, as it could happen in the case of condition monitoring applications, the torque used to pre-calculate meshing stiffness should agree with that used for the dynamic simulation, giving inaccurate results otherwise.

6.2. The effect of bearing clearances and friction forces

Having demonstrated the ability of the model to take into account the torque level, in this section it was used to characterize the role of bearing clearances and friction forces, and their interaction under several load levels, in the resulting dynamic behavior. Four cases were considered as a preliminary test to discern the impact of each aspect on the final vibratory signature (see Table 4).

Table 4: Scenarios for dynamic simulations

Case No.	Bearing clearance	Gear friction forces
1	Yes	No
2	Yes	Yes
3	No	No
4	No	Yes

In the first case, simulations were done considering bearing clearances (no pre-loads) while gear friction forces were removed (friction coefficient null). In the second case, simulations were carried out considering bearing clearances (no pre-load) combined with friction forces (considering several friction coefficients). In the third case, bearing pre-loads (no clearances) were introduced while gear friction forces were once more time removed from the simulations (friction coefficient null). Finally, in the fourth case, bearing pre-loads (no clearance) and gear friction forces were combined.

6.2.1. Bearing clearance without gear friction forces

The resultant orbits obtained in the dynamic simulations for a bearing cycle, after removing the initial transient, are presented in Figure 7. In contrast with the results obtained in quasi-static analysis, dynamic terms provide orbits with higher amplitude in the LOA. This fact can be appreciated with more detail in Figures 8(a) and 8(b), where it is presented the orbit for one cycle of the $1b1$ bearing when the applied torque is 10 Nm and 100 Nm. The symbols ($\circ$) and ($\square$) represent the beginning and end point of the orbit for a bearing period respectively.

Moreover, it can be observed how bearing compliances change for each bearing interact with gear mesh excitation, providing several oscillations for a bearing cycle. Regarding the DTE, the results obtained for a gear cycle running at 1000 rpm under several torque loads are presented in Figure 9. As the torque rises, the DTE is shifted up, as a consequence of the additional kinematical turn required to close the contact when the gear center distance is increased due to the shaft and bearing flexibilities. This phenomenon, together with the tooth deflection determines the start and end time of contact between successive teeth pairs, and therefore the resultant DTE. The DTE obtained with the lowest torque (see Figure 10(a)) exhibit a remarkable oscillation at the (BPF). The corresponding angular period is determined from Eq.(6), substituting the cage rotation to the angle between rolling elements and solving the angle rotated by the inner ring under the assumption that it

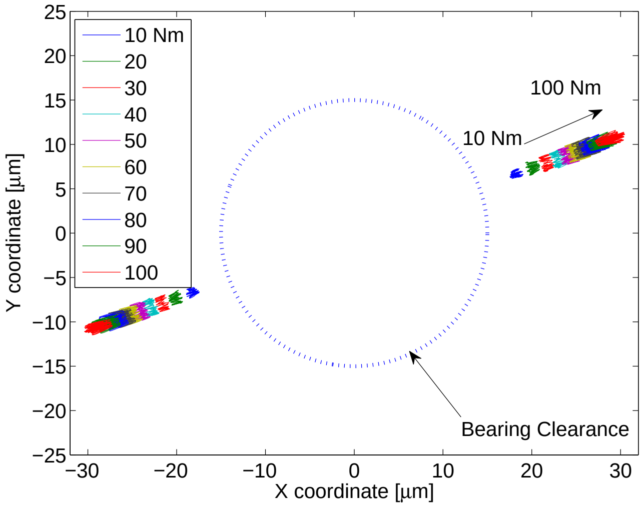

Figure 7: Bearing 1b1 and 2b1 center orbits with several transmitted torques. Dashed line depicts bearing clearance

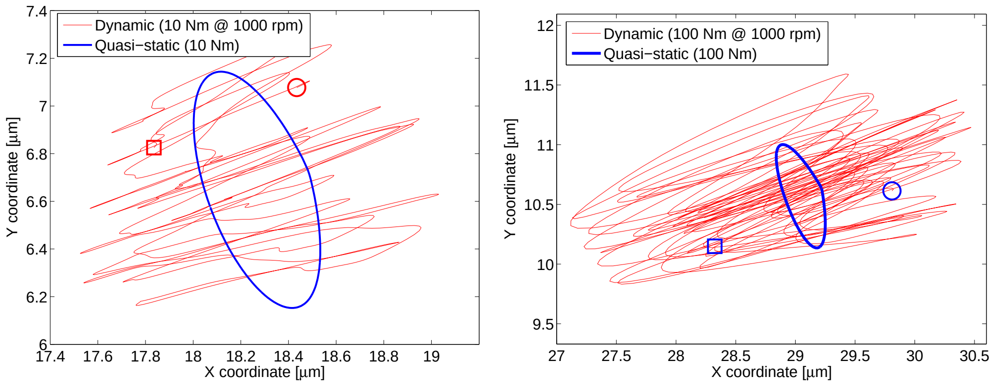

(a) Torque 10 Nm

(b) Torque 100 Nm.

Figure 8: Bearing 1b1 center orbit for quasi-static (blue) and dynamic analysis at 1000 rpm (red)

is fixed to the gear shaft and that the outer ring is fixed to the case.

After substitution of the values corresponding to the bearing listed in Table 3, the number of bearing cycles per gear turn is 3.6342. Figures 10(a) and 10(b) shows the bearing periods corresponding to a gear turn for the extreme values of the transmitted torque. Otherwise, when the torque be-

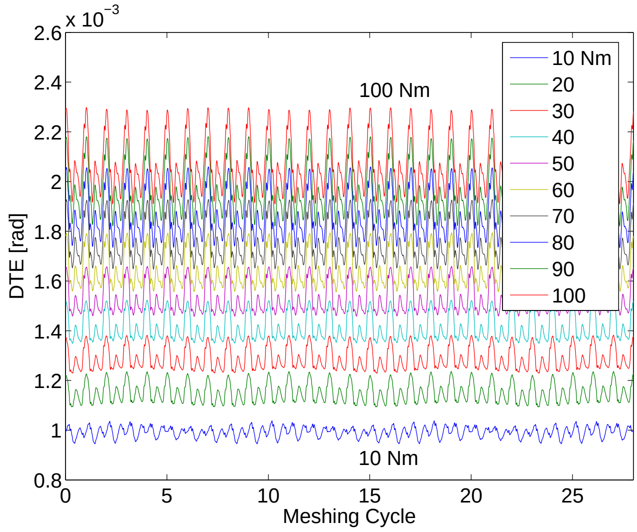

Figure 9: DTE at 1000 rpm for several torque loads

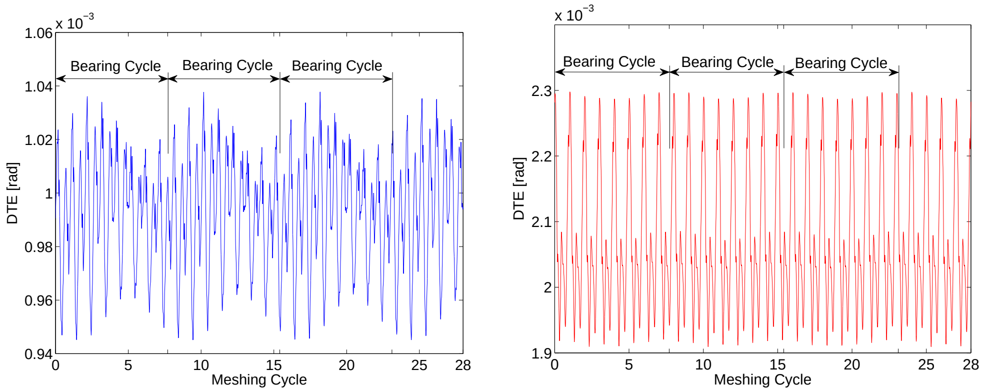

(a) Torque 10 Nm

(b) Torque 100 Nm

Figure 10: DTE for a gear turn running at 1000 rpm

comes higher, the effect of bearing variable compliance is lessened, being more difficult to discern its presence on the DTE record (see Figure 10(b)). In fact, smoothed amplitudes for ball pass frequency are commonly expected, because the effective slipping at the rolling contacts gives place to random fluctuations on the cage frequency even for stationary input speed. Thus the vibration energy is spread in the frequency domain, and the corresponding peaks are masked by the random noise. Moreover, the application of bearing preloads removes the bearing clearance, reducing the amplitude of the variable bearing compliance and therefore the magnitude of the corresponding harmonics.

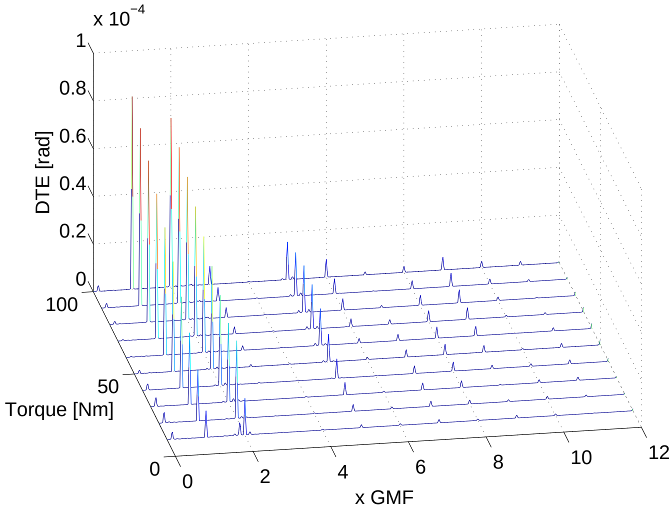

Figure 11: DTE spectra for several torque loads

The corresponding linear spectrum for the torque range analyzed is presented as a waterfall diagram in Figure 11. There, the main peaks appear at the GMF and its harmonics but also it is possible to appreciate a little peak corresponding to the BPF, which is more noticeable for low torques.

Regarding the force transmitted through the bearings to the case, Figure 12 shows the waterfall spectrum of the forces at the bearing designated as $1b1$ in Figure 1 (bearing 1 on shaft 1) in the LOA. As with the DTE, two excitation frequencies can be appreciated due to GMF and BPF, being dominant the harmonics of the GMF. Up to three harmonics of the BPF can be discerned at the low frequency range but also as lateral sidebands of the GMF harmonics. As the transmitted torque increases, the amplitude of GMF harmonics rises but there are changes in their relative importance. Thus, for low torque values up to 40 Nm the dominant harmonic is the second one, while for higher torques the 5^{th} becomes the highest. On the other side, BPF harmonics show a reduction for torques of 60 and 70 Nm. This fact is consistent with the amplitude of the orbit in the LOA obtained in the quasi-static analysis shown in Figure 3. The BPF in the low frequency range will be lower in real machinery because the slipping at the rolling contacts

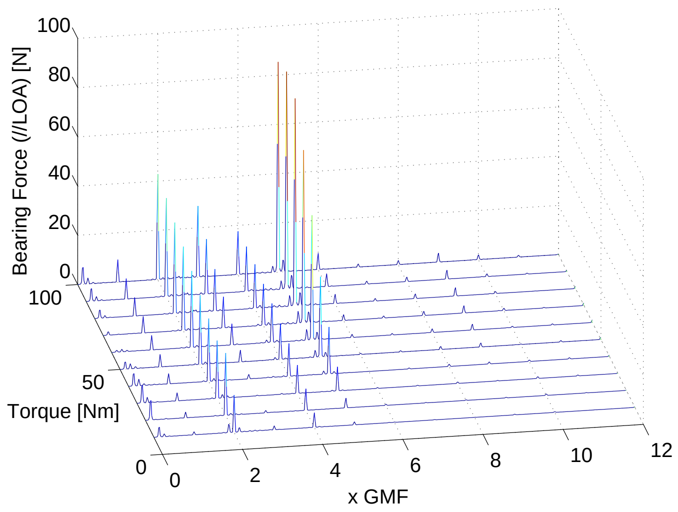

Figure 12: LOA Bearing force (1b1) spectra for several torques

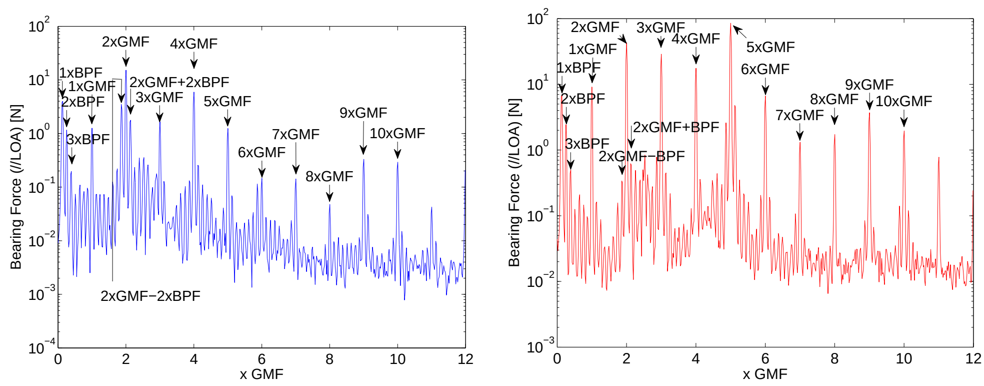

(a) Torque 10 Nm

(b) Torque 100 Nm

Figure 13: Bearing 1b1 LOA force spectrum

yields to a non-stationary behavior and as a consequence the BPF energy is spread in the vicinity band and masked by the noise floor. Obviously, although the amplitude of all harmonics is generally increased as the torque rises, that increment has a different shape for each harmonic because of the non-linear changes on the parametric excitation due to the gear meshing stiffness and its interaction with bearing variable compliance. This aspect shows the importance of having a torque dependent model for on condition monitoring.

A more detailed view of the $1b1$ LOA force spectra for 10 and 100 Nm is presented in Figure 13, where the force amplitude was represented in log-scale to discern better the consequences of the BPF modulations. As it was remarked previously for the lowest torque (Figure 13(a)), the highest amplitude corresponds to the 2^{nd} GMF harmonic while it corresponds to the 5^{th} for the maximum assessed torque (Figure 13(b)).

6.2.2. Bearing clearance with gear friction forces

In the following, friction efforts combined with bearing clearances and preloads are analyzed with the aim to better understand the role played by these factors on the gear transmission dynamics and particularly on the vibratory magnitudes under stationary conditions. To carry out this task, the original model was modified including the friction efforts and dynamic simulations were done again with the same set up for the integration algorithm and working conditions. Two friction coefficients have been considered: 0.03 and 0.05. From the point of view of the bearing center orbits, the differences are clear as it can be seen in Figure 14.

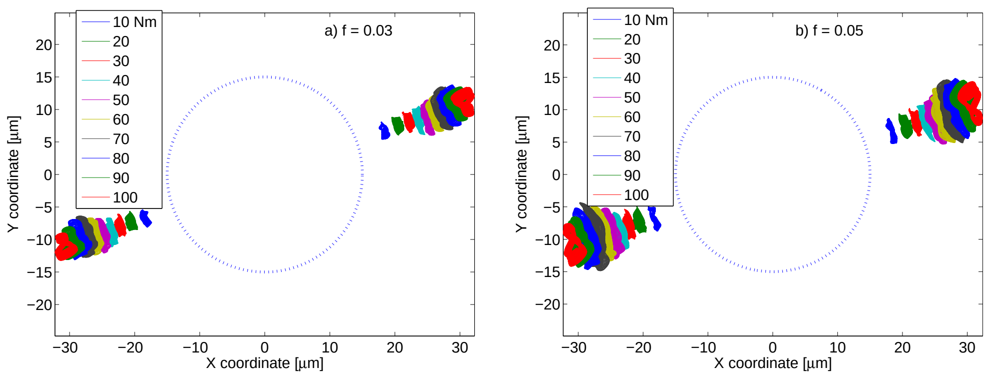

(a) f=0.03 (b) f=0.05

Figure 14: Bearing $1b1$ and $2b1$ center orbits at 1000 rpm, with several transmitted torques (dashed line depicts the bearing clearance.)

Due to bearing clearance, OLOA bearing stiffness is lower than in the LOA direction, and as a consequence the orbits are spread on the OLOA for quasi-static analysis. Nevertheless, when dynamic simulations are carried out this fact becomes masked by the longest displacements in the LOA (see Figure 7 and Figure 8). Friction forces enlarge the OLOA's displacements of bearing centers and as a consequence gears present a swinging motion governed by the bearing clearance. As the friction coefficient increases, this phenomenon is more evident and the OLOA's displacements grow. To have a better insight of the orbit origin, in Figure 15 the orbits obtained for bearing $1b1$ are presented, corresponding to the extreme values of the torque range (10 and 100 Nm) for $f = 0$, 0.03 and 0.05.

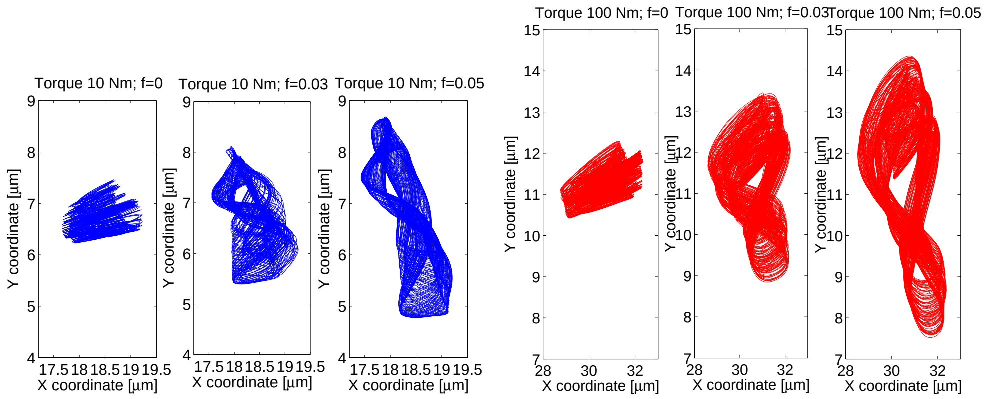

(a) 10 Nm (b) 100 Nm

Figure 15: Detail of the Bearing 1b1 Orbit at 1000 rpm and three friction coefficients 0 (left column); 0.03 (middle column) and 0.05 (Right column)

More interesting conclusions can be drawn from the spectral decomposition of the bearing forces. In the case of the LOA in Figure 16, the most evident change is the generalized increment in the amplitude of sidebands around the GMF at the BPF as the friction coefficient raises. This increment is particularly large around the 2^{nd}, 3^{th} and the 4^{th} GMF harmonics. This behavior can be explained by the excitation of both translational modes located between 472-1130 Hz and 1291-2000 Hz in the load range considered in the simulation (see Table 5). The reader can find more details about this modes in [34] where the authors identify the natural frequencies and modal shapes of the same transmission, linearizing the model by averaging the compliance of bearings and gears along a cycle.

As a consequence resonant frequencies change notably as a function of the torque and this change is more evident in the modes where bearing stiffness plays an important role. These modes involve translational motions and appear in pairs one for normal direction (LOA) and one for tangential direction (OLOA). For each pair, the tangential ones (OLOA) have lower

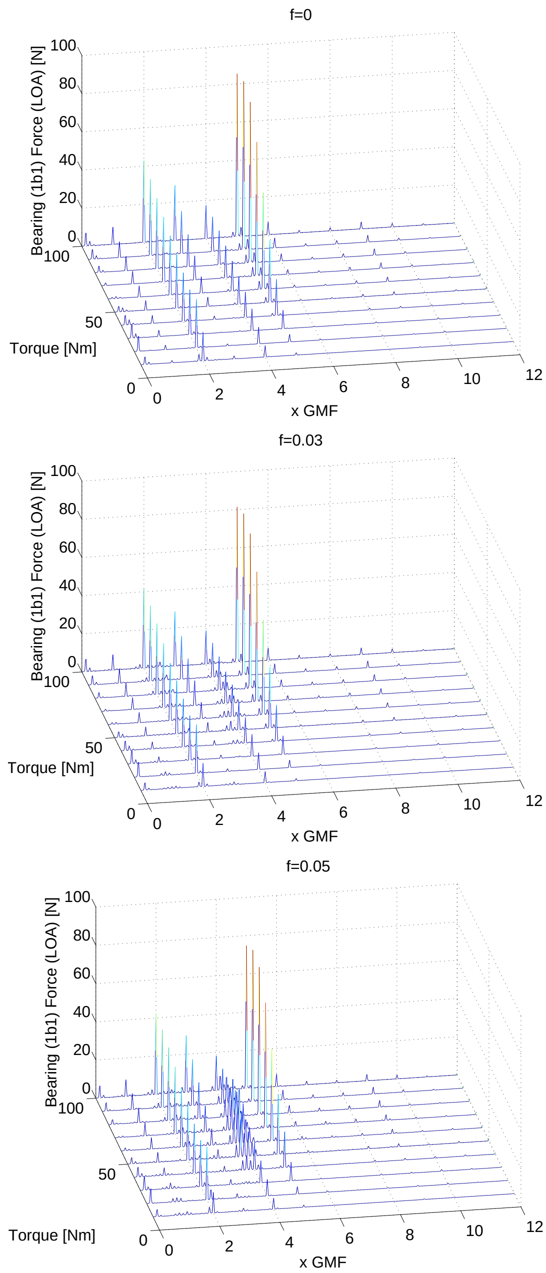

Figure 16: Amplitude spectrum of the Bearing $1b1$ LOA force at 1000 rpm for several torques

Table 5: Natural frequencies and mode type with bearing clearance under several transmitted torques. Modes were classified as: Rotational R, Translational T and Mixed Modes R-T.

Mode	Freq (Hz) 10 Nm	Freq (Hz) 50 Nm	Freq (Hz) 100 Nm	Mode Type
1	411	770	913	R1-T
2	472	922	1130	Tt1
3	1061	1384	1523	R1-T
4	1291	1775	2000	Tn1
5	1966	2175	2307	R1-T
6	4284	4320	4339	R2-T
7	5909	6003	6056	R3-T
8	6562	6650	6709	Tt2
9	6605	6706	6771	R3-T
10	6763	6967	7083	Tn2
11	6867	7074	7193	R3-T
12	9701	9763	9806	Tt3
13	9739	9819	9863	R3-T
14	9847	10008	10107	Tn3
15	9972	10122	10215	R3-T
16	14382	14382	14382	R4
17	14702	14702	14702	R5
18	15744	15745	15746	R6
19	15938	15947	15952	R7

frequencies because of the less stiffness in this direction as a consequence of bearing clearance.

Due to the speed used for simulations (1000 rpm), 2^{nd}, 3^{th} and the 4^{th} GMF harmonics match with 2^{nd} and 4^{th} modes for a certain range of the applied torque. As a consequence the sidebands around these GMF peaks raise particularly near the fourth one, as in this case the mode involves translation into the LOA (subscript n means normal movement that is LOA).

On the other side, the spectra in the OLOA (the tangential direction in the mode classification) presented in Figure 17 shows a generalized increment of the GMF amplitude particularly from the 1^{st} to the 3^{th} when friction forces are considered in simulations. Furthermore, friction forces amplify the lateral sidebands at the BPF, particularly around the 2^{nd} GMF harmonic which excites the 2^{nd} mode involving motion in the OLOA direction.

6.2.3. Bearing pre-loads (no clearance) without gear friction forces

In this section the role of bearing preloads on the behavior of bearings and their consequences on the transmission dynamics have been analyzed in order to assess the performance of the developed model. Introducing bearing preloads is accomplished by assigning a negative value for clearance in Eq.(8). Thus, rolling elements become in contact even when there is no

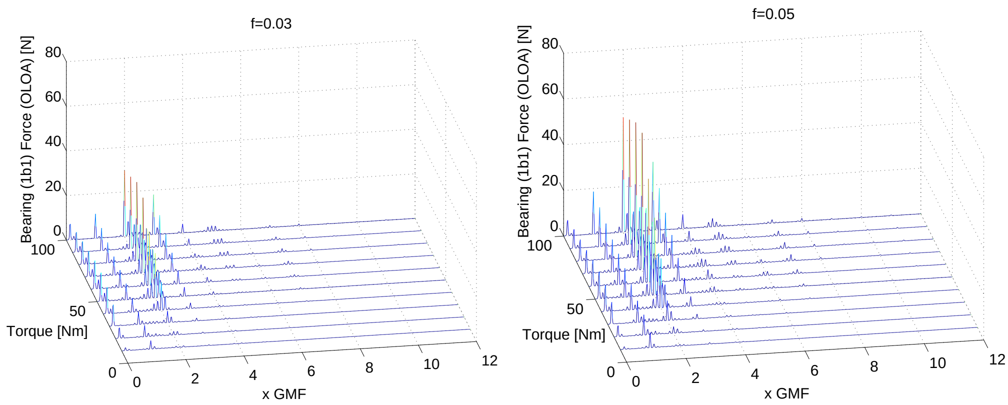

(a) $f = 0.03$ (b) $f = 0.05$

Figure 17: Amplitude spectrum of the Bearing $1b1$ OLOA force at 1000 rpm for several torques

torque applied to the transmission. The main consequence is that average bearing stiffness in LOA remains close to the case without preload while OLOA become higher. Therefore the orbit amplitude is roughly the same in the meshing direction (LOA) but is shortened in the tangential direction (OLOA). This fact can be observed in Figure 18 where the results were obtained using a negative value for the clearance equal to 0.001 mm. Bearing preload constraint the orbit centroid at the inner area of the circle defined by the nominal clearance, which is represented to facilitate comparison with the simulations where clearance was considered. This constraint reduces the average value of the Loaded Transmission Error due to the consequent minor variation on the gear center distance with respect to the nominal, caused by the reduced backlash (see Figure 19) shifting down the Loaded Transmission Error curves. Furthermore, it can be appreciated a lower modulation of the meshing phenomena by the ball pass frequency of the bearing which is much more evident for low transmitted torques when clearances are present.

As a consequence it can be observed the lateral sidebands disappearance at the BPF around the GMF harmonics in the amplitude spectrum of the bearing transmitted forces. Meanwhile, the low frequency harmonics at the BPF are strongly attenuated (see Figure 20). To facilitate the comparison the spectra corresponding to a torque of 100 Nm of the 1b1 LOA force when clearance and preload were considered are presented in log-scale in Figure 21.

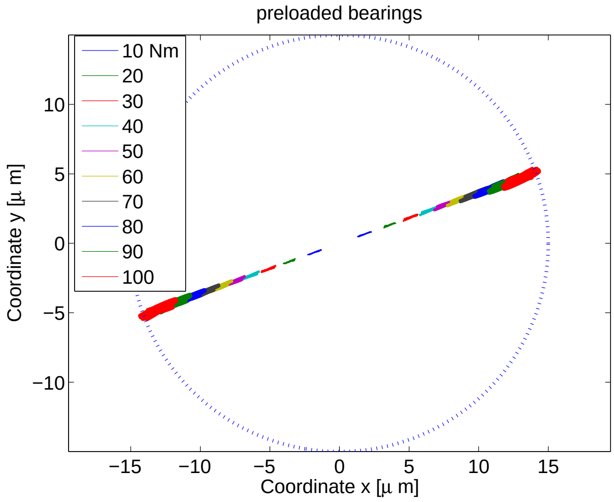

Figure 18: Bearing $1b1$ and $2b1$ center orbits at 1000 rpm, with several transmitted torques with preload bearing preload (c=-0.001 mm). Dashed line depicts bearing clearance

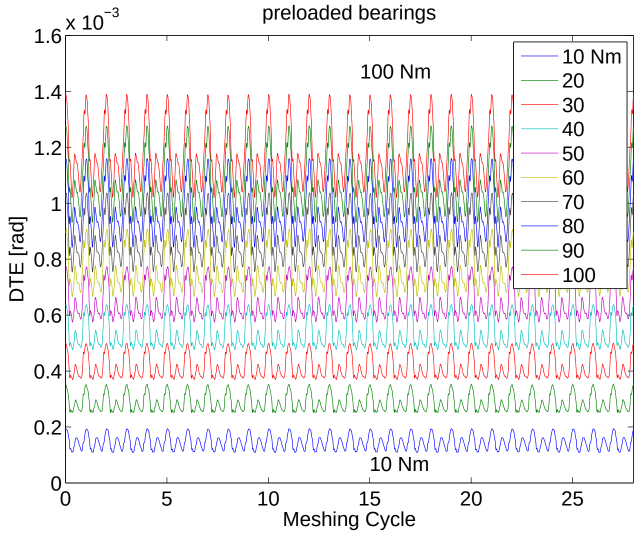

Figure 19: DTE at 1000 rpm for several torques with bearing preload (c=-0.001 mm)) for two levels of transmitted torque (Dashed line 10 Nm; Solid line 100 Nm)

6.2.4. Bearing pre-loads (no clearance) and gear friction forces

When preload and friction are combined in simulations the resulting orbits are those shown in Figure 22. As it was observed under the no preload

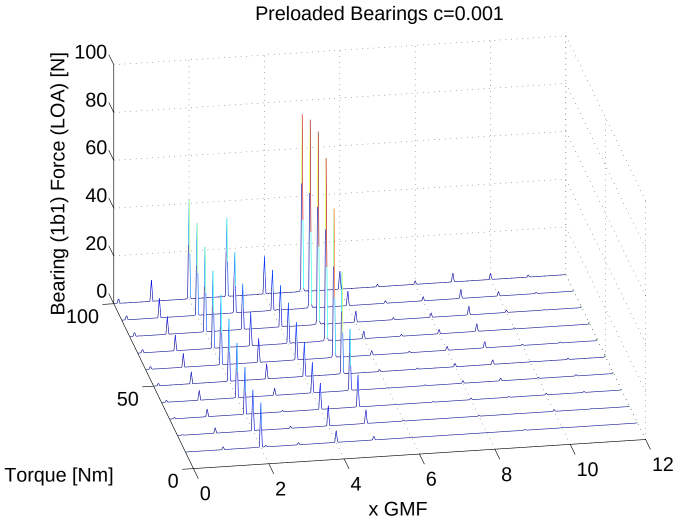

Figure 20: Amplitude spectrum of the Bearing 1b1 LOA force at 1000 rpm for several torques and bearing preload (c=-0.001 mm)

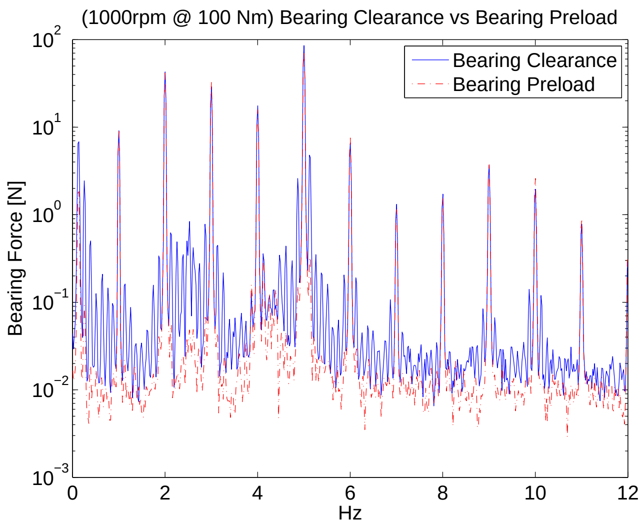

Figure 21: Comparison of amplitude spectrum of the Bearing 1b1 LOA force at 1000 rpm @ 100 Nm, with clearance and with preload (c=-0.001 mm)

case, friction leads to a magnification of the OLOA's displacements, which is even more evident as the friction coefficient rises. Nevertheless, due to the bearing preload, OLOA's lateral bearing stiffness increases, preventing the characteristic swinging motion observed when bearing clearances exist.

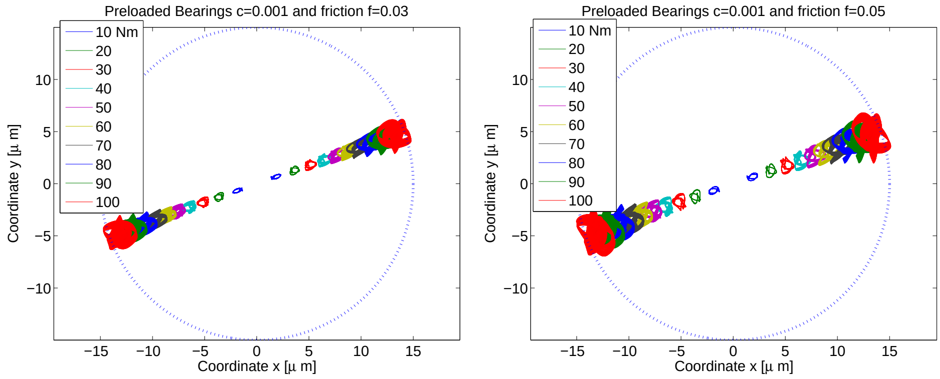

(a) $f = 0.03$ (b) $f = 0.05$

Figure 22: Bearing $1b1$ and $2b1$ center orbits at 1000 rpm, working under several transmitted torques, with bearing preload

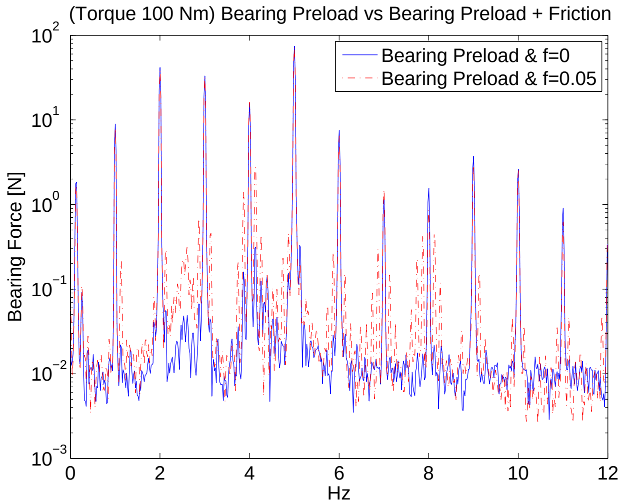

Figure 23: Comparison of amplitude spectrum of bearing $1b1$ LOA force at 1000 rpm @ 100 Nm, with preload and with (red-dashdot) and without friction (blue-solid)

With respect to Loaded Transmission Error and bearing forces, time records follow a similar pattern as that obtained with preloads. The most important consequence of friction force was the increment of the amplitude

Table 6: Natural frequencies and mode type with preload under several transmitted torques. Modes were classified as: Rotational R, Translational T and Mixed Modes R-T.

Mode	Freq (Hz) 10 Nm	Freq (Hz) 50 Nm	Freq (Hz) 100 Nm	Mode Type
1	981	1097	1158	R1-T
2	1431	1626	1766	Tt1
3	1476	1705	1864	R1-T
4	1507	1826	2036	Tn1
5	2091	2245	2362	R1-T
6	4294	4328	4347	R2-T
7	5932	6026	6080	R3-T
8	6816	6898	6963	Tt2
9	6833	6926	7000	R3-T
10	6847	6993	7103	Tn2
11	6970	7121	7230	R3-T
12	9887	9952	10005	Tt3
13	9900	9977	10038	R3-T
14	9911	10029	10124	Tn3
15	10050	10161	10246	R3-T
16	14382	14382	14382	R4
17	14702	14702	14702	R5
18	15744	15745	15746	R6
19	15938	15947	15952	R7

of lateral sidebands at the BPF around the GMF harmonics, as it was also observed in the case of bearing clearances.

This fact can be appreciated in Figure 23 where the spectra in log-scale with and without friction are compared when preloads are considered in the simulations. It is remarkable the amplitude increment of the BPF sidebands around the 3^{rd}, 4^{th} but also on 7^{th} and 8^{th} GMF harmonics.

As preloads involve an increment of the bearing stiffness, particularly in the OLOA, natural frequencies corresponding to the lower modes becomes higher, as it can be observed in Table 6. As a consequence, sideband activity at the BPF is shifted to the 3^{rd} and 4^{th} GMF harmonics as they are located in the range between 1431-1766 Hz and 1507-2036 Hz, where the translational modes are excited.

More evident changes can be appreciated in the OLOA direction by comparison with respect to the case with bearing clearance, particularly in the presence of friction. In Figure 24 it can be observed the presence of peaks at the 3^{rd} and the 4^{th} GMF harmonic when bearing preloads were included in the analysis. In contrast, when clearances were considered, it was the 2^{nd} GMF harmonic which became the most important. Moreover, in the OLOA the BPF modulation appears clearly independently of the load and friction, in opposite to the attenuation observed in the LOA.

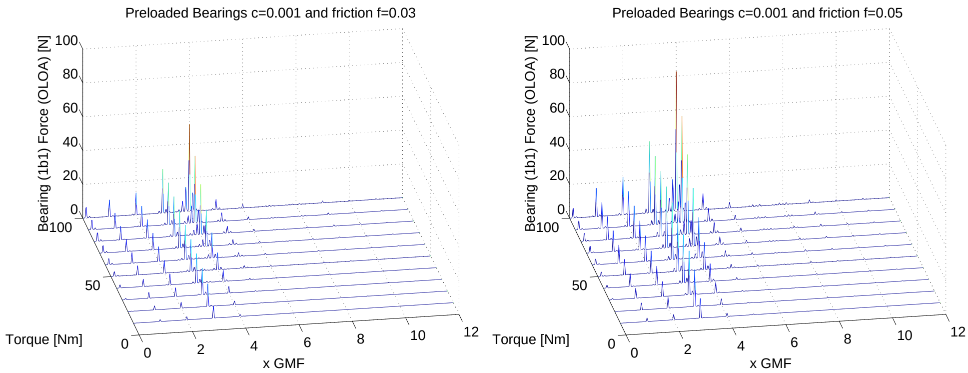

(a) $f = 0.03$ (b) $f = 0.05$

Figure 24: Amplitude spectrum of the Bearing 1b1 OLOA force at 1000 rpm for several torques, with bearing preload (c=-0.001 mm) and friction

7. Conclusions

Gear transmissions remain as one of the most complex mechanical systems from the point of view of noise and vibration behavior. Research on gear modeling leading to the obtaining of models capable of accurately reproduce the dynamic behavior of real gear transmissions has spread out the last decades. Most of these models, although useful for design stages, often include simplifications that impede their application for condition monitoring purposes. Trying to filling this gap, the model presented in this paper allows to simulate gear transmission dynamics including most of these features usually neglected by the state of the art models.

The developed model is capable of considering simultaneously the internal excitations due to the variable meshing stiffness (including the coupling among successive tooth pairs in contact, the non-linearity linked with the contacts between surfaces and the dissipative effects), and those excitations consequence of the bearing variable compliance (including clearances or preloads). Another strong feature of the modeling approach is the fact that it allows for the simulation of gear dynamics in a realistic torque dependent scenario.

Torque level has a direct impact on the amplitude of GMF harmonics, for which non-torque dependent models would provide dramatically different spectral decompositions of measured transmitted forces in an on condition monitoring application. In contrast, the proposed method simulates the dynamic behavior under different torque levels, observing significant changes in the amplitude of the GMF harmonics as a result of the excitation of transverse vibration modes in the LOA. As a consequence the forces at bearing level show that GMF harmonics present changes not only in their absolute amplitudes but also in their relative importance for each applied load. This fact is due to the non-linearity involved on both gears and bearings, providing different resonant frequencies depending on the transmitted load.

The inclusion of dissipative effects in the modeling approach allows for the consideration of the friction meshing forces. The model is capable of simulate different scenarios in which it can be shown that friction forces magnify BPF sidebands in the transmitted forces signal in the LOA and even more clearly in the OLOA due to the extension of the gear center orbit in this direction.

The model is also capable of showing the differences that would be encountered in the vibratory signal of a gear transmission either preloads are included or not in the bearing support. As the simulation results point out, the gear orbit amplitude when preload is considered is shortened in the OLOA direction, remaining similar for the LOA direction, thus reducing the Loaded Transmission Error and resulting in the lateral sidebands disappearance at the BPF around the GMF harmonics in the spectrum of the measured bearing transmitted forces.

In view of the results, the proposed model constitutes a valuable starting point to develop on condition monitoring tools. Further work should be done in order to assess the behavior on non-stationary conditions.

References

[1] I. Energetics, Gear industry vision, (Accessed July 2015) (2004). URL `http://agma.server294.com/images/uploads/gearvision.pdf`

[2] F. Oyague, Gearbox modeling and load simulation of a baseline 750-kw wind turbine using state-of-the-art simulation codes, Tech. Rep. NREL/TP-500-41160, NREL (2009).

[3] W. Bartelmus, Mathematical modelling and computer simulations as an aid to gearbox diagnostics, Mechanical Systems and Signal Processing 15 (5) (2001) 855–871.

[4] D. Ho, R. Randall, Optimisation of bearing diagnostic techniques us-

ing simulated and actual bearing fault signals, Mechanical Systems and Signal Processing 14 (5) (2000) 763–788.

[5] I. Howard, S. Jia, J. Wang, The dynamic modelling of a spur gear in mesh including friction and a crack, Mechanical Systems and Signal Processing 15 (5) (2001) 831–853.

[6] F. Chaari, T. Fakhfakh, M. Haddar, Analytical modelling of spur gear tooth crack and influence on gearmesh stiffness, European Journal of Mechanics, A/Solids 28 (3) (2009) 461–468.

[7] O. Mohammed, M. Rantatalo, J.-O. Aidanp, Dynamic modelling of a one-stage spur gear system and vibration-based tooth crack detection analysis, Mechanical Systems and Signal Processing 54 (2015) 293–305.

[8] F. Chaari, W. Baccar, M. Abbes, M. Haddar, Effect of spalling or tooth breakage on gearmesh stiffness and dynamic response of a one-stage spur gear transmission, European Journal of Mechanics, A/Solids 27 (4) (2008) 691–705.

[9] S. Jia, I. Howard, Comparison of localised spalling and crack damage from dynamic modelling of spur gear vibrations, Mechanical Systems and Signal Processing 20 (2) (2006) 332–349.

[10] H. Endo, R. Randall, G. C., Differential diagnosis of spall vs. cracks in the gear tooth fillet region: Experimental validation, Mechanical Systems and Signal Processing 23 (3) (2009) 636–651.

[11] A. Kahraman, R. Singh, Non-linear dynamics of a spur gear pair, Journal of Sound and Vibration 142 (1) (1990) 49–75.

[12] P. K. Gupta, Transient ball motion and skid in ball bearings, Journal of Tribology 97 (2) (1975) 261–269.

[13] S. Fukata, E. H. Gad, T. Kondou, T. Ayabe, H. Tamura, On the radial vibration of ball bearings. (computer simulation)., Bulletin of the JSME 28 (239) (1985) 899–904.

[14] R. Singh, T. C. Lim, Vibration transmission through rolling element bearings in geared rotor systems, Tech. Rep. 90-C-019, NASA (1990).

[15] F. Lahmar, P. Velex, Simulations of gear-rolling element bearing interactions in geared transmissions, in: Proceedings of the ASME Design Engineering Technical Conference, Vol. 4 A, 2003, pp. 315–324.

[16] P. Velex, M. Maatar, A mathematical model for analyzing the influence of shape deviations and mounting errors on gear dynamic behaviour, Journal of Sound and Vibration 191 (5) (1996) 629–660.

[17] N. Sawalhi, R. B. Randall, Simulating gear and bearing interactions in the presence of faults. Part I. the combined gear bearing dynamic model and the simulation of localised bearing faults, Mechanical Systems and Signal Processing 22 (8) (2008) 1924–1951.

[18] F. Viadero, A. Fernandez del Rincon, R. Sancibrian, P. Garcia, A. de Juan, A model of spur gears supported by ball bearings, in: WIT Transactions on Modelling and Simulation, Vol. 46, 2007, pp. 711–722.

[19] A. Fernandez del Rincon, F. Viadero, M. Iglesias, P. Garcia, A. de Juan, R. Sancibrian, A model for the study of meshing stiffness in spur gear transmissions, Mechanism and Machine Theory 61 (2013) 30–58.

[20] A. Fernandez del Rincon, F. Viadero, M. Iglesias, A. de Juan, P. Garcia, R. Sancibrian, Effect of cracks and pitting defects on gear meshing, Proceedings of the Institution of Mechanical Engineers, Part C, Journal of Mechanical Engineering Science 226(11) (2012) 2805–2815.

[21] A. Fernandez del Rincon, M. Iglesias, A. de Juan, P. Garcia, R. Sancibrian, F. Viadero, Gear transmission dynamic: Effects of tooth profile deviations and support flexibility, Applied Acoustics 77 (2014) 138–149.

[22] A. Fernandez del Rincon, M. Iglesias, A. de Juan, A. Diez-Ibarbia, P. Garca, F. Viadero, Gear transmission dynamics: Effects of index and run out errors, Applied Acoustics (2015) –.

[23] C. Gosselin, L. Cloutier, Q. D. Nguyen, A general formulation for the calculation of the load sharing and transmission error under load of spiral bevel and hypoid gears, Mechanism and Machine Theory 30 (3) (1995) 433–450.

[24] R. G. Parker, S. M. Vijayakar, T. Imajo, Non-linear dynamic response of a spur gear pair: modelling and experimental comparisons, Journal of Sound and Vibration 237 (3) (2000) 435–455.

[25] L. Vedmar, A. Andersson, A method to determine dynamic loads on spur gear teeth and on bearings, Journal of Sound and Vibration 267 (5) (2003) 1065–1084.

[26] M. Iglesias, A. Fernandez del Rincon, A. de Juan, A. Diez-Ibarbia, P. Garcia, F. Viadero, Advanced model for the calculation of meshing forces in spur gear planetary transmissions, Meccanica 50 (7) (2015) 1869–1894.

[27] A. Hammami, A. Fernandez Del Rincon, F. Chaari, M. Iglesias, F. Viadero, M. Haddar, Effects of variable loading conditions on the dynamic behaviour of planetary gear with power recirculation, Measurement (2016) –doi:http://dx.doi.org/10.1016/j.measurement.2016.07.083.

[28] S. He, Effect of sliding friction on spur and helical gear dynamics and vibro-acoustics, Ph.D. thesis, The Ohio State University (2008).

[29] R. Kasuba, J. W. Evans, Extended model for determining dynamic loads in spur gearing., Journal of mechanical design 103 (2) (1981) 398–409.

[30] S. Theodossiades, O. Tangasawi, H. Rahnejat, Gear teeth impacts in hydrodynamic conjunctions promoting idle gear rattle, Journal of Sound and Vibration 303 (35) (2007) 632–658.

[31] E. Mucchi, G. Dalpiaz, A. Rivola, Elastodynamic analysis of a gear pump. Part II: Meshing phenomena and simulation results, Mechanical Systems and Signal Processing 24 (7) (2010) 2180–2197.

[32] M. P. Koster, Vibrations of Cam Mechanism, McMillan Press, 1974.

[33] T. Harris, M. Kotzalas, Rolling Bearing Analysis, John Wiley & Sons Inc, 2001.

[34] A. Fernandez del Rincon, F. Viadero, M. Iglesias, P. Garcia, A. de Juan, R. Sancibrian, Load effects on the dynamics of spur gear transmissions, ASME Conference Proceedings 2010 (49194) (2010) 369–378.

[35] B. Hamrock, B. Jacobson, S. Schmid, Fundamentals of Fluid Film Lubrication, 2nd Edition, 1994.

Annex A: Dynamic Equations

Based on the description given in section 2 and on Figure 1 the governing equations of motion for each element considered in the sample transmission were derived as follows.

$$\dot{\theta}_{In} = \omega \tag{A. 1}$$

$$\begin{aligned}
m_{1b1}\ddot{x}_{1b1} &+C_{1b1G1}(\dot{x}_{1b1} - \dot{x}_{1G1}) + C_{1b1}(\dot{x}_{1b1})+ \\
&+K_{1b1G1}(x_{1b1} - x_{1G1}) + f_{1b1x}(q_{1b1}) = 0; \\
m_{1b1}\ddot{y}_{1b1} &+C_{1b1G1}(\dot{y}_{1b1} - \dot{y}_{1G1}) + C_{1b1}(\dot{y}_{1b1})+ \\
&+K_{1b1G1}(y_{1b1} - y_{1G1}) + f_{1b1y}(q_{1b1}) = 0; \\
J_{1b1}\ddot{\theta}_{1b1} &+C_{T1J1b1}(\dot{\theta}_{1b1} - \dot{\theta}_{In}) + C_{T1b1G1}(\dot{\theta}_{1b1} - \dot{\theta}_{1G1})+ \\
&+K_{T1J1b1}(\theta_{1b1} - \theta_{In}) + K_{T1b1G1}(\theta_{1b1} - \theta_{1G1}) = 0;
\end{aligned} \tag{A. 2}$$

$$\begin{aligned}
m_{1b2}\ddot{x}_{1b2} &+C_{1G1b2}(\dot{x}_{1b2} - \dot{x}_{1G1}) + C_{1b2}(\dot{x}_{1b2})+ \\
&+K_{1G1b2}(x_{1b2} - x_{1G1}) + f_{1b2x}(q_{1b2}) = 0; \\
m_{1b2}\ddot{y}_{1b2} &+C_{1G1b2}(\dot{y}_{1b2} - \dot{y}_{1G1}) + C_{1b2}(\dot{y}_{1b2})+ \\
&+K_{1G1b2}(y_{1b2} - y_{1G1}) + f_{1b2y}(q_{1b2}) = 0; \\
J_{1b2}\ddot{\theta}_{1b2} &+C_{T1G1b2}(\dot{\theta}_{1b2} - \dot{\theta}_{1G1}) + K_{T1G1b2}(\theta_{1b2} - \theta_{1G1}) = 0;
\end{aligned} \tag{A. 3}$$

$$\begin{aligned}
m_{2b1}\ddot{x}_{2b1} &+C_{2b1G1}(\dot{x}_{2b1} - \dot{x}_{2G1}) + C_{2b1}(\dot{x}_{2b1})+ \\
&+K_{2b1G1}(x_{2b1} - x_{2G1}) + f_{2b1x}(q_{2b1}) = 0; \\
m_{2b1}\ddot{y}_{2b1} &+C_{2b1G1}(\dot{y}_{2b1} - \dot{y}_{2G1}) + C_{2b1}(\dot{y}_{2b1})+ \\
&+K_{2b1G1}(y_{2b1} - y_{2G1}) + f_{2b1y}(q_{2b1}) = 0; \\
J_{2b1}\ddot{\theta}_{2b1} &+C_{T2b1G1}(\dot{\theta}_{2b1} - \dot{\theta}_{2G1}) + K_{T2b1G1}(\theta_{2b1} - \theta_{2G1}) = 0;
\end{aligned} \tag{A. 4}$$

$$\begin{aligned}
m_{2b2}\ddot{x}_{2b2} &+C_{2G1b2}(\dot{x}_{2b2}-\dot{x}_{2G1})+C_{2b2}(\dot{x}_{2b2})+\\
&+K_{2G1b2}(x_{2b2}-x_{2G1})+f_{2b2x}(q_{2b2})=0;\\
m_{2b2}\ddot{y}_{2b2} &+C_{2G1b2}(\dot{y}_{2b2}-\dot{y}_{2G1})+C_{2b2}(\dot{y}_{2b2})+\\
&+K_{2G1b2}(y_{2b2}-y_{2G1})+f_{2b2y}(q_{2b2})=0;\\
J_{2b2}\ddot{\theta}_{2b2} &+C_{T2b2J2}(\dot{\theta}_{2b2}-\dot{\theta}_{2J2})+C_{T2G1b2}(\dot{\theta}_{2b2}-\dot{\theta}_{2G1})+\\
&+K_{T2b2J2}(\theta_{2b2}-\theta_{2J2})+K_{T2G1b2}(\theta_{2b2}-\theta_{2G1})=0;
\end{aligned} \tag{A. 5}$$

$$\begin{aligned}
m_{1G1}\ddot{x}_{1G1} &+C_{1b1G1}(\dot{x}_{1G1}-\dot{x}_{1b1})+C_{1G1b2}(\dot{x}_{1G1}-\dot{x}_{1b2})+\\
&+K_{1b1G1}(x_{1G1}-x_{1b1})+K_{1G1b2}(x_{1G1}-x_{1b2})+\\
&+f_{1G12G1x}(q_{1G1},q_{2G1},\dot{q}_{1G1},\dot{q}_{2G1})=0;\\
m_{1G1}\ddot{y}_{1G1} &+C_{1b1G1}(\dot{y}_{1G1}-\dot{y}_{1b1})+C_{1G1b2}(\dot{y}_{1G1}-\dot{y}_{1b2})+\\
&+K_{1b1G1}(y_{1G1}-y_{1b1})+K_{1G1b2}(y_{1G1}-y_{1b2})+\\
&+f_{1G12G1y}(q_{1G1},q_{2G1},\dot{q}_{1G1},\dot{q}_{2G1})=0;\\
J_{1G1}\ddot{\theta}_{1G1} &+C_{T1b1G1}(\dot{\theta}_{1G1}-\dot{\theta}_{1b1})+C_{T1G1b2}(\dot{\theta}_{1G1}-\dot{\theta}_{1b2})+\\
&+K_{T1b1G1}(\theta_{1G1}-\theta_{1b1})+K_{T1G1b2}(\theta_{1G1}-\theta_{1b2})+\\
&+f_{1G12G1\theta}(q_{1G1},q_{2G1},\dot{q}_{1G1},\dot{q}_{2G1})=0;
\end{aligned} \tag{A. 6}$$

$$\begin{aligned}
m_{2G1}\ddot{x}_{2G1} &+C_{2b1G1}(\dot{x}_{2G1}-\dot{x}_{2b1})+C_{2G1b2}(\dot{x}_{2G1}-\dot{x}_{2b2})+\\
&+K_{2G1b2}(x_{2G1}-x_{2b2})+K_{2b1G1}(x_{2G1}-x_{2b1})+\\
&+f_{2G11G1x}(q_{1G1},q_{2G1},\dot{q}_{1G1},\dot{q}_{2G1})=0;\\
m_{2G1}\ddot{y}_{2G1} &+C_{2b1G1}(\dot{y}_{2G1}-\dot{y}_{2b1})+C_{2G1b2}(\dot{y}_{2G1}-\dot{y}_{2b2})+\\
&+K_{2G1b2}(y_{2G1}-y_{2b2})+K_{2b1G1}(y_{2G1}-y_{2b1})+\\
&+f_{2G11G1y}(q_{1G1},q_{2G1},\dot{q}_{1G1},\dot{q}_{2G1})=0;\\
J_{2G1}\ddot{\theta}_{2G1} &+C_{T2b1G1}(\dot{\theta}_{2G1}-\dot{\theta}_{2b1})+C_{T2G1b2}(\dot{\theta}_{2G1}-\dot{\theta}_{2b2})+\\
&+K_{T2b1G1}(\theta_{2G1}-\theta_{2b1})+K_{T2G1b2}(\theta_{2G1}-\theta_{2b2})+\\
&+f_{2G11G1\theta}(q_{1G1},q_{2G1},\dot{q}_{1G1},\dot{q}_{2G1})=0;
\end{aligned} \tag{A. 7}$$

$$J_{2J2}\ddot{\theta}_{2J2}+C_{T2b2J2}(\dot{\theta}_{2J2}-\dot{\theta}_{2b2})+K_{T2b2J2}(\theta_{2J2}-\theta_{2b2})=T_{Out}; \tag{A. 8}$$

Where m_{iEj} and J_{iEj} represent respectively translational and rotational inertia lumped at the center of the element j belonging to the shaft i. Meanwhile, the stiffness and damping associated with the flexural behavior of the connecting shafts between the different elements (Ej and Ek) becomes defined

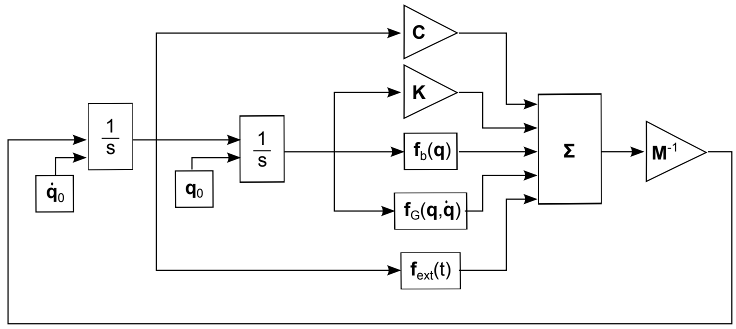

Figure A. 1: Flow diagram for equation A. 9

by K_{iEjEk} and C_{iEjEk}, while subscript T is added to distinguish torsional properties. Moreover, C_{ibj} describes the viscous damping associated with the bearing j belonging to the shaft i, and $f_{ibj}(q_{ibj})$ provides the force on bearing b_j belonging to the shaft i while $f_{iGjkGt}(q_{iGj}, q_{kGt})$ gives the meshing forces on shaft i due to the contact of gear Gj on shaft i with gear Gt on shaft k. As friction and damping are included in the meshing formulation, the corresponding function requires the gear center positions and also the first derivatives.

Then, mass, damping and stiffness matrices for the whole system (shafts, gears and bearings) are assembled into the dynamic matrix equation defined in Eq.(1). Numerical integration of dynamic equations was done combining Matlab and Simulink® tools. For this purpose, the general equation Eq.(1) was reformulated for its implementation in Simulink® environment arriving at the following expression:

$$\ddot{\mathbf{q}} = \mathbf{M}^{-1}\left(\mathbf{f}_{Ext}(t) - \mathbf{C}\dot{\mathbf{q}} - \mathbf{K}\mathbf{q} - \mathbf{f}_b(\mathbf{q}) - \mathbf{f}_G(\mathbf{q}, \dot{\mathbf{q}})\right); \qquad \text{(A. 9)}$$

Fig. A. 1 shows the flow diagram corresponding to Eq.(A. 9). There, function blocks with ad-hoc Matlab® functions were used for the non-linear terms due to gears and bearings while *ode45* solver was used for numerical integration.

Annex B: Bearing contact stiffness (k_{RE})

Hertzian theory considers the contact between two bodies (hereinafter designated as A and B) with curved surfaces subjected to a load F. The surface of each contacting body is represented by two ellipsoids defined by the radii of curvature in two perpendicular planes ($r_{A1}, r_{A2}, r_{B1}, r_{B2}$) adopting the negative sign for concave surfaces. In this work, only angular contact ball bearings are considered. Thus, the radii of curvature for inner contact are defined by:

$$r_{A1} = r_{A2} = \frac{d}{2}; \qquad r_{B1} = R_i; r_{B2} = \; - r_i \tag{B. 1}$$

While for the contact with the outer race, the radii of curvature are:

$$r_{A1} = r_{A2} = \frac{d}{2}; \qquad r_{B1} = -R_o; r_{B2} = \; - r_o \tag{B. 2}$$

Where the subscript A refers to the rolling element while subscript B is applied for the track, R_i and R_o are the radii defined in Figure 2 whereas r_i and r_o are the curvature radii of each race channel. Then, the curvature sum and difference [33] are defined by:

$$\sum \rho = \frac{1}{r_{A1}} + \frac{1}{r_{A2}} + \frac{1}{r_{B1}} + \frac{1}{r_{B2}} \tag{B. 3}$$

$$F(\rho) = \frac{\left(\frac{1}{r_{A1}} - \frac{1}{r_{A2}}\right) + \left(\frac{1}{r_{B1}} - \frac{1}{r_{B2}}\right)}{\sum \rho} \tag{B. 4}$$

The application of the classical Hertz theory requires the resolution of complete elliptic integrals of first and second kind $\mathfrak{F}$ y $\mathfrak{E}$. To avoid this inconvenience, in the case of bearings made of steel the approximate relationships derived by Hamrock *et al.* [35] for steel bodies can be used, so that:

$$\delta_B = 2,79 \cdot 10^{-4} \delta^* \cdot \left(\sum \rho\right)^{1/3} Q^{2/3} \tag{B. 5}$$

Where δ is the contact deflection in mm, Q is the load applied expressed in N and δ^* is a dimensionless parameter which can be obtained from Table 7, as a function of the difference of curvature $F(\rho)$. Solving for the force Q in Eq.(B. 5) and identifying terms, the contact stiffness value (k_C) is expressed as:

$$k_C = \left(2.15 \cdot 10^5 \delta^{*-3/2} \left(\sum \rho\right)^{-1/2}\right); \qquad \frac{N}{mm^{3/2}} \tag{B. 6}$$

Then, the total hertzian stiffness for a single ball in contact with both races is obtained by serial composition of the individual stiffness obtained

Table 7: Dimensionless contact deformation (δ^*) as a function of the curvature difference (extracted from [33])

$F(\rho)$	(δ^*)	$F(\rho)$	(δ^*)	$F(\rho)$	(δ^*)
0	1	0.83495	0.7602	0.995112	0.3176
0.1075	0.9974	0.87366	0.7169	0.997300	0.2705
0.3204	0.9761	0.90999	0.6636	0.9981847	0.2427
0.4795	0.9429	0.936738	0.6112	0.9989156	0.2106
0.5916	0.9077	0.95738	0.5551	0.9994785	0.17167
0.6716	0.8733	0.97290	0.4960	0.9998527	0.11995
0.7332	0.8394	0.983797	0.4352	1	0
0.7948	0.7961	0.990902	0.3745		

for inner and outer races (k_{Ci}, k_{Co}), taking into account the nonlinear relationship between force and displacement (through the exponent p):

$$k_B = \frac{k_{Ci} k_{Co}}{\left(k_{Ci}^{1/p} + k_{Co}^{1/p} \right)^p} \tag{B. 7}$$

Acknowledgements

The authors would like to acknowledge Project DPI2013 − 44860 funded by the Spanish Ministry of Science and Technology and Project PRX14/00451 funded by the Spanish Ministry of Education, Culture and Sports.